# Optimization-Driven Design of a Kinesthetic Haptic Interface with Human-Like Capabilities

Michael Fennel, Antonio Zea, Uwe D. Hanebeck

***Abstract*— Developing manipulators for kinesthetic haptic interfaces is challenging due to a large number of design parameters. We propose a novel optimization-driven design approach taking into account the properties of the entire workspace of the human arm instead of a specific task. To achieve this, models of both the human arm and the haptic manipulator are derived and deployed in a suitable objective function, which simultaneously considers poses, velocities, accelerations, as well as displayed forces and torques. A detailed analysis and experiments with real-world motion tracking data show that the proposed method is capable of finding meaningful design parameters to enable good haptic transparency.**

***Index Terms*— Kinesthetic Devices, System Design and Analysis, Human Factors and Ergonomics**

## I. Introduction

The human arm is an astonishing manipulator due to its high versatility, power-to-weight ratio, and dexterity. While this is great for the daily life of humans, it causes serious challenges in the design of kinesthetic haptic interfaces. Hence, a vast number of interfaces for specific tasks were developed in the past. Although these systems share the goal of force rendering, they differ regarding the workspace size, the number of contact points, the available degrees of freedom (DOF), and mobility. Thus, their applicability is very limited in foreign scenarios. This might be an acceptable disadvantage for cost-sensitive applications, but in the context of research, a general-purpose haptic interface as depicted in Fig. 1 is more appealing. To build such a device without any assumptions about the tasks to be performed, common base requirements for all application scenarios must be established.

Traditionally, the interaction of humans with their environment is achieved with the human hand. For this reason, the human arm, including shoulder and hand, is selected as the common denominator in the following. This raises the non-trivial question, how an optimal design for a kinesthetic haptic interface, which has capabilities comparable to the human arm, must look like. We answer this question by presenting a new optimization-driven design method for non-redundant kinesthetic haptic interfaces with a given kinematic structure. The resulting haptic transparency is maximized by taking into account the workspace of the human arm, the achievable velocities and accelerations, as well as the ability to display defined forces and torques.

This work was supported by the ROBDEKON project of the German Federal Ministry of Education and Research, and the state of Baden-Württemberg through bwHPC.

All authors are with the Intelligent Sensor-Actuator-Systems Laboratory (ISAS), Institute for Anthropomatics and Robotics, Karlsruhe Institute of Technology (KIT), Germany michael.fennel@kit.edu, antonio.zea@kit.edu, uwe.hanebeck@kit.edu.

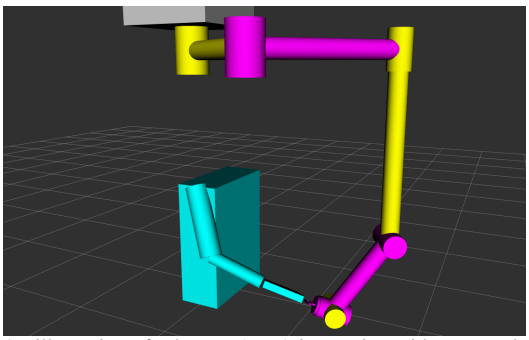

Fig. 1: An illustration of a human (cyan) interacting with a general-purpose kinesthetic haptic interface (magenta/yellow).

## II. Related Work

The idea of creating a universal haptic interface for the human arm has been addressed before. For example, in [1] a group of general-purpose haptic devices is presented. Although these are quite versatile, the design process is not based on how well a device will work with a human in the quantitative sense. Similarly, in [2] the anatomical properties of the human shoulder are only incorporated qualitatively into the design of an exoskeleton. A thorough analysis of the arm movements that need to be covered by an exoskeleton can be found in [3]. However, the obtained data is mainly used for heuristic optimizations. To objectively compare different installations of the same haptic interface, a kinematic model of the human arm is utilized in [4]. The drawback here is that this method is neither capable of optimizing the haptic manipulator itself nor does it consider any dynamic properties.

Of course, the design of haptic interfaces can be interpreted as a common manipulator design problem. A well-known approach is Yoshikawa's manipulability index and its variants [5], [6]. While the concept is straightforward, it cannot be directly applied to manipulator optimization due to its locality. Instead, global optimization-driven methods such as [7] or [8] can be applied to maximize global isotropy. This looks appealing at first but ignores the properties of the human arm entirely. Another path is taken by [9], where the design of robotic legs is formulated as a task-dependent optimization problem. For the initially stated problem, task information is not available and so the method cannot be applied directly.

## III. Coordinate Systems and Notation

Throughout this paper, positions and translations are denoted with $\underline{x}$. The corresponding velocities and accelerations are denoted with $\underline{v}$ and $\underline{a}$, respectively. For orientations, rotation matrices $\mathbf{C}$ are used together with angular velocities $\underline{\omega}$ and accelerations $\dot{\underline{\omega}}$. Poses are expressed as pairs $(\underline{x},\mathbf{C})$ or as homogeneous transformation matrices $\mathbf{T}$.

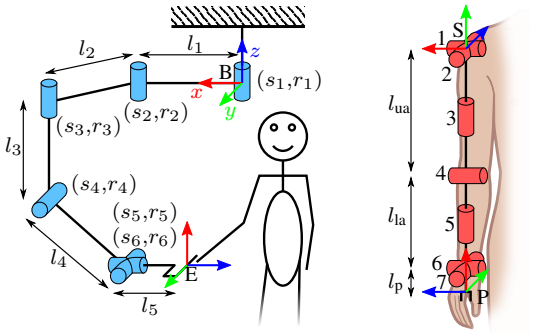


(a) Haptic manipulator. (b) Right human arm.

Fig. 2: Illustration of the models used throughout this paper.

| Joint $i$ | $q_i^{\mathrm{m}}$ | $d_i^{\mathrm{m}}$ | $a_i^{\mathrm{m}}$ | $\alpha_i^{\mathrm{m}}$ |
|---|---|---|---|---|
| 1 | $q_1^{\mathrm{m}}$ | 0 | $l_1$ | 0 |
| 2 | $q_2^{\mathrm{m}}$ | 0 | $l_2$ | 0 |
| 3 | $q_3^{\mathrm{m}}+180°$ | $-l_3$ | 0 | 90° |
| 4 | $q_4^{\mathrm{m}}-90°$ | 0 | $l_4$ | 0 |
| 5 | $q_5^{\mathrm{m}}+90°$ | 0 | 0 | 90° |
| 6 | $q_6^{\mathrm{m}}$ | $l_5$ | 0 | 0 |

TABLE I: DH parameters of the haptic manipulator.

Joint angles $\underline{q}$ and joint torques $\underline{\tau}$ are utilized in conjunction with the end effector Jacobian $\mathbf{J}$ and the joint space inertia matrix $\mathbf{H}$ to describe a kinematic chain. For translational and rotational quantities, superscripts denote the reference coordinate frame in which a quantity is expressed, whereas subscripts indicate a point or a frame of interest. For example, $\mathbf{x}_B^A$ represents the position of frame $B$ given in coordinates of frame $A$. Quantities that do not depend on a frame but either refer to the human arm "h" or the robotic manipulator "m" are distinguished with the corresponding letter in the superscript. To reference the $i$-th entry of a vector or to address row $i$ and column $j$ of a matrix, $i$ or $i,j$ are included in the subscript.

In the remainder, the coordinate frames from Fig. 2 are used. The frames S in the shoulder and P in the palm represent the base and the end effector of the human arm model. Moreover, the base and the end effector of the haptic manipulator are denoted with B and E, respectively.

## IV. Problem Statement

The design of a haptic interface and manipulator has countless parameters and various design stages. For this reason, we will narrow down the problem in the following.

### A. Manipulator Model

The design of the manipulator that is going to be optimized is assumed to be known a priori except for some finite set of parameters. In this paper, the example in Fig. 2(a) with six electrically actuated rotational joints and the Denavit-Hartenberg (DH) parameters from Table I is studied. Although this choice might look arbitrary at first glance, it can be motivated with some background knowledge about (haptic) manipulator design. According to [4] and [10], haptic interfaces with an enclosing configuration are preferable because collisions are less likely and the workspace overlap between the haptic manipulator and the user is maximized. Hence, the first three joints in Fig. 2(a) are chosen as a SCARA-like configuration moving above the user. To enable height and inclination adjustments with a minimal number of joints, a vertical SCARA-like configuration with two joints is added. A sixth joint, whose axis intersects the axis of joint 5, is placed at the end of the kinematic chain for rolling motions. As a result, end effector movements with 6 DOF with a minimal number of joints are enabled, while the inverse kinematics (IK) is still simple to calculate. The resulting partial symmetry with the human wrist and its three intersecting axes constitutes an additional biological motivation for the choice of the last two joints.

In addition to the link lengths $\underline{l} \in \mathbb{R}^5$, the joint sizes $\underline{s} \in S^6$ and the joint gear ratios $\underline{r} \in R^6$, selected from the discrete set of sizes $S$ and transmissions $R$, are included as yet unknown parameters in the model. Based on the look-up tables $f_{\dot{q}}$, $f_\tau$, and $f_m$, the maximum angular velocity $\dot{q}_{i,\max}^{\mathrm{m}} = f_{\dot{q}}(s_i,r_i)$, the maximum torque $\tau_{i,\max}^{\mathrm{m}} = f_\tau(s_i,r_i)$, and the mass $m_i^{\mathrm{m}} = f_m(s_i)$ are then defined for joint $i$.

### B. Goal

The goal of the proposed algorithm is to find an *optimal* set of design parameters $\underline{p} = (\underline{l}^{\mathsf{T}},\underline{s}^{\mathsf{T}},\underline{r}^{\mathsf{T}})^{\mathsf{T}}$ for the previously described manipulator. Optimal here means, that the resulting manipulator covers the workspace of the human arm as much as possible regarding the reachable poses, velocities, and accelerations to achieve maximal haptic transparency. Furthermore, forces and torques need to be displayed with the haptic user interface. Due to the absence of a specific task, it is reasonable to include the coverage of isotropic forces and torques with a given worst-case magnitude during the optimization. It is obvious that these goals are contradicting. For example, long link lengths are in general beneficial for the workspace size and the achievable velocities. However, this will yield low acceleration and force capabilities at the end effector if the available joint torques are not increased. For this reason, it is crucial to find a good trade-off between the different properties of the resulting manipulator.

## V. Human Arm Analysis

Before the *coverage* of a haptic interface can be optimized, it is necessary to study the capabilities of the human arm. Therefore, the considered human arm model is examined here.

### A. Kinematic Model

To obtain a simple model of the human arm, the shoulder girdle is assumed to be fixed. Then, the arm can be approximated with a serial manipulator with seven independent rotational degrees of freedom as illustrated in Fig. 2(b). Following the discussion in [4], the spherical glenohumeral (i.e., shoulder) joint is modeled using joints 1 to 3 representing abduction/adduction, flexion/extension, and interior/exterior rotation, respectively. The elbow flexion/extension is modeled with joint 4. The wrist movements are replicated using joints 5 to 7 representing forearm pronation/supination, wrist flexion/extension, and radial/ulnar deviation in that order. This model is completed with the tool center point in the center of the palm, which yields the DH parameters in Table II. The emerging link lengths $l_{\mathrm{ua}} = 326\mathrm{mm}$, $l_{\mathrm{la}} = 256\mathrm{mm}$, and $l_{\mathrm{p}} = 95\mathrm{mm}$ are derived from the statistical model reported in [11] and the median body height of males [12].[1] The height of the glenohumeral joint over ground is then $1.43\mathrm{m}$.

[1] Male data was preferred over female data, since females are statistically smaller, resulting in shorter and therefore less challenging arm lengths.

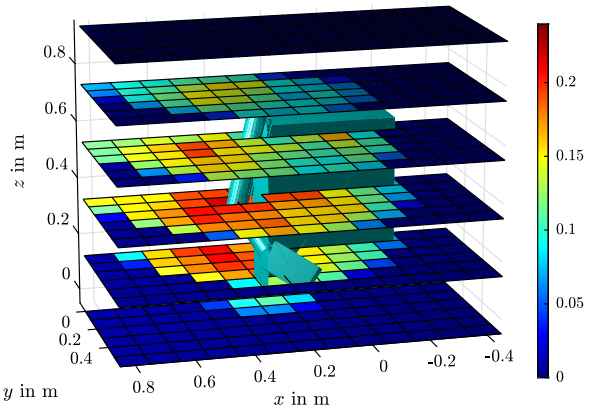


Fig. 3: Visualization of the cardinality of the pose-dependent sets of IK solutions $Q^{\mathrm{h}}(\mathbf{T}_{\mathrm{P}}^{\mathrm{S}})$ after integration over all rotations $W_{\mathrm{rot}}$ and normalization with respect to $|W_{\mathrm{rot}}|$ . The red regions mark positions, where the human arm exhibits high dexterity, and hence regions that are important to reach.

Each joint in the model has joint limits, for which different values are stated in literature. With this information, a meaningful set of joint limits was selected manually in Table II, taking into account that extreme movements overhead or behind the torso are not considered. In addition to kinetostatic modelling, the maximal joint velocities $\underline{\dot{q}}^{\mathrm{h}}_{\mathrm{max}}$ and accelerations $\underline{\ddot{q}}^{\mathrm{h}}_{\mathrm{max}}$ from [13] are included in Table II. Although these values are not necessarily a true upper bound as the human arm is capable of extreme movements, they can be interpreted as an upper bound for activities of daily life.

### B. Workspace

The first step in finding an optimal haptic manipulator is a workspace analysis of the human arm. In this paper, a sample-based analysis is suggested as it will preserve local information that can be exploited later during the optimization. The translational part of the workspace around the shoulder is sampled with an orthogonal lattice resulting in the set of discrete positions $W_{\mathrm{tran}} \subset \mathbb{R}^3$. In addition, all orientations in $SO(3)$ are sampled deterministically and near-uniformly from the 3-hyperhemisphere (i.e., the set of unambiguous unit quaternions) using a Fibonacci grid in $\mathbb{R}^3$ [16] and a conformal mapping with constant Jacobian determinant. This yields the set $W_{\mathrm{rot}}$. Thus, the cross product $W = W_{\mathrm{tran}} \times W_{\mathrm{rot}} \subset SE(3)$ describes the set of examined poses. For each pose $\mathbf{T}_{\mathrm{P}}^{\mathrm{S}} = \left(\underline{x}_{\mathrm{P}}^{\mathrm{S}}, \mathbf{C}_{\mathrm{P}}^{\mathrm{S}}\right) \in W$, the IK solutions of the human arm are calculated after joint 3 is discretized equidistantly between its limits to incorporate the kinematic redundancy of the human arm. To keep the number of human arm configurations computationally tractable, only the solution with the highest manipulability index [5] is retained for each pose. As a result, the empty or one-element set of IK solutions $Q^{\mathrm{h}}(\mathbf{T}_{\mathrm{P}}^{\mathrm{S}})$ for a specific pose is obtained. A visualization of this set is depicted in Fig. 3. The total number of reachable poses in $W$, which is required later, is defined as $n^{\mathrm{h}}_{\mathrm{reach}}$.

### C. Velocity and Acceleration Capabilities

From robot kinematics, it is well known that

$$\begin{pmatrix} \underline{\omega}_{\mathrm{P}}^{\mathrm{ST}} & \underline{\dot{x}}_{\mathrm{P}}^{\mathrm{ST}} \end{pmatrix}^{\mathsf{T}} = \mathbf{J}^{\mathrm{h}}\left(\underline{q}^{\mathrm{h}}\right) \underline{\dot{q}}^{\mathrm{h}} \tag{1}$$

relates joint velocities and end effector velocities of a kinematic chain. An ideal haptic manipulator should be able

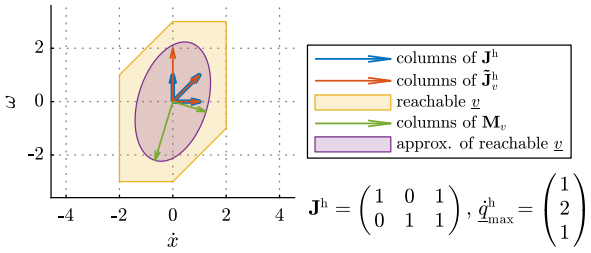


Fig. 4: Illustration of the reachable set of velocities for a manipulator with 3 joints. The principal axes of the velocity ellipsoid are a reasonable approximation for the set of reachable end effector velocities.

of reproducing all end effector velocities of the human arm. To test this goal, all possible end effector velocities could be calculated based on the joint velocity limits and checked, but this is computationally expensive. For this reason, we approximate the possible velocities at a given $\underline{q}^{\mathrm{h}}$ with the principal axes of the 6-dimensional velocity ellipsoid as illustrated in Fig. 4. This is achieved by first scaling the columns of $\mathbf{J}^{\mathrm{h}}$ with the maximal joint velocities according to

$$\tilde{\mathbf{J}}_v^{\mathrm{h}} = \mathbf{J}^{\mathrm{h}}\left(\underline{q}^{\mathrm{h}}\right) \mathrm{diag}\left(\underline{\dot{q}}^{\mathrm{h}}_{\mathrm{max}}\right). \tag{2}$$

Then, the singular value decomposition (SVD)

$$\tilde{\mathbf{J}}_v^{\mathrm{h}} = \mathbf{U}_v \mathbf{S}_v \mathbf{V}_v^{\mathsf{T}} \tag{3}$$

is calculated. Here, $\mathbf{U}_v \in \mathbb{R}^{6\times 6}$ and $\mathbf{V}_v \in \mathbb{R}^{7\times 7}$ are orthonormal matrices, while $\mathbf{S}_v \in \mathbb{R}^{6\times 7}$ is a diagonal matrix. Due to the SVD properties, the columns of

$$\mathbf{M}_v = \mathbf{U}_v \mathbf{S}_v \tag{4}$$

contain the desired principal axes of the end effector velocity ellipsoid. In a similar way, the acceleration capabilities can be calculated. The time derivative of (1) is

$$\begin{pmatrix} \dot{\underline{\omega}}_{\mathrm{P}}^{\mathrm{ST}} & \ddot{\underline{x}}_{\mathrm{P}}^{\mathrm{ST}} \end{pmatrix}^{\mathsf{T}} = \dot{\mathbf{J}}^{\mathrm{h}} \underline{\dot{q}}^{\mathrm{h}} + \mathbf{J}^{\mathrm{h}} \underline{\ddot{q}}^{\mathrm{h}}. \tag{5}$$

With the assumption that the highest accelerations usually occur at low velocities, the first term can be neglected and (5) can be approximated with

$$\begin{pmatrix} \dot{\underline{\omega}}_{\mathrm{P}}^{\mathrm{ST}} & \ddot{\underline{x}}_{\mathrm{P}}^{\mathrm{ST}} \end{pmatrix}^{\mathsf{T}} \approx \mathbf{J}^{\mathrm{h}} \underline{\ddot{q}}^{\mathrm{h}}. \tag{6}$$

Due to the form of this equation, which is identical to (1),

$$\tilde{\mathbf{J}}_a^{\mathrm{h}} = \mathbf{J}^{\mathrm{h}} \mathrm{diag}\left(\underline{\ddot{q}}^{\mathrm{h}}_{\mathrm{max}}\right) = \mathbf{U}_a \mathbf{S}_a \mathbf{V}_a^{\mathsf{T}} \text{and} \tag{7}$$

$$\mathbf{M}_a = \mathbf{U}_a \mathbf{S}_a \tag{8}$$

hold. The matrices $\mathbf{U}_a$, $\mathbf{S}_a$, and $\mathbf{V}_a$ originate from the SVD of $\tilde{\mathbf{J}}_a^{\mathrm{h}}$ and have the same properties as $\mathbf{U}_v$, $\mathbf{S}_v$, and $\mathbf{V}_v$. Analog to $\mathbf{M}_v$, the columns of $\mathbf{M}_a$ contain the principal axes that approximate the accelerations, which are feasible with the given human arm model.

## VI. Manipulator Design

Based on the analysis of the human arm, the actual optimization process of the manipulator design with the parameter vector $\underline{p}$ is explained in the following. Although the following elaborations deal with the example from Section IV-A, an application for arbitrary non-redundant serial manipulators with 6 DOF is also feasible. Parallel kinematics are not covered without adaptions due to the occurring constraint torques.

| | DH Parameters | | | | Joint Limits in ° | | | | | | | | | |
|---|---|---|---|---|---|---|---|---|---|---|---|---|---|---|
| | | | | | [14] | | [13] | | [15] | | selected | | | |
| Joint $i$ | $q_i^{\mathrm{h}}$ | $d_i^{\mathrm{h}}$ | $a_i^{\mathrm{h}}$ | $\alpha_i^{\mathrm{h}}$ | min | max | min | max | min | max | min | max | $\dot{q}_{i,\max}^{\mathrm{h}}$ in $^\circ\mathrm{s}^{-1}$ [13] | $\ddot{q}_{i,\max}^{\mathrm{h}}$ in $^\circ\mathrm{s}^{-2}$ [13] |
| 1 | $q_1^{\mathrm{h}}+90^\circ$ | 0 | 0 | $90^\circ$ | -30 | 180 | -14 | 134 | -50 | 180 | -30 | 90 | 172 | 1312 |
| 2 | $q_2^{\mathrm{h}}+90^\circ$ | 0 | 0 | $90^\circ$ | -50 | 180 | -18 | 62 | -30 | 130 | -50 | 90 | 137 | 950 |
| 3 | $q_3^{\mathrm{h}}$ | $-l_{\mathrm{ua}}$ | 0 | $-90^\circ$ | -80 | 80 | -72 | 55 | -90 | 60 | -80 | 80 | 141 | 1049 |
| 4 | $q_4^{\mathrm{h}}$ | 0 | 0 | $90^\circ$ | 0 | 145 | 42 | 163 | 0 | 160 | 0 | 160 | 173 | 1266 |
| 5 | $q_5^{\mathrm{h}}-90^\circ$ | $-l_{\mathrm{la}}$ | 0 | $90^\circ$ | -90 | 85 | $-^*$ | $-^*$ | -85 | 80 | -90 | 85 | 486 | 4344 |
| 6 | $q_6^{\mathrm{h}}+90^\circ$ | 0 | 0 | $-90^\circ$ | -85 | 85 | -40 | 55 | -80 | 90 | -85 | 85 | 233 | 2790 |
| 7 | $q_7^{\mathrm{h}}$ | 0 | $-l_{\mathrm{p}}$ | 0 | -45 | 15 | $-^*$ | $-^*$ | -30 | 15 | -45 | 15 | 204 | 2476 |

TABLE II: Parameters of the human arm model for the right arm. The joint limits are compiled from different sources. The last four columns hold the selected joint angle limits, the maximal joint velocities, and the maximal joint accelerations, respectively. Asterisks mark implausible data that was omitted.

### A. Objective Function

The core of the optimization procedure is the objective function. As outlined before, there are various contradicting goals, when it comes to designing a manipulator. Since no objective shall be preferred in advance, we propose to utilize the sum of equally weighted objectives

$$J(\underline{p}) = J_x + J_v + J_a + J_f, \tag{9}$$

where $J_x$, $J_v$, $J_a$, and $J_f$ represent the *pose coverage*, the *velocity coverage*, the *acceleration coverage*, and the *force/torque coverage*, respectively. The equal weighting is ensured by normalizing each term's value to the interval $[0,1]$, so that a value of 1 indicates an ideal manipulator.

*1) Pose Coverage:* The number of palm poses of the human arm that can be reached by the manipulator's end effector is

$$n_{\mathrm{reach}}^{\mathrm{m}} = \sum_{\mathbf{T}_{\mathrm{P}}^{\mathrm{S}} \in W} \left| Q^{\mathrm{m}}\left(\mathbf{T}_{\mathrm{E}}^{\mathrm{B}}, \underline{p}\right) \right|, \tag{10}$$

where $Q^{\mathrm{m}}\left(\mathbf{T}_{\mathrm{E}}^{\mathrm{B}}, \underline{p}\right)$ is the empty or one-element set of IK solutions of the manipulator under design with $\mathbf{T}_{\mathrm{E}}^{\mathrm{B}} = \mathbf{T}_{\mathrm{S}}^{\mathrm{B}} \mathbf{T}_{\mathrm{P}}^{\mathrm{S}} \mathbf{T}_{\mathrm{E}}^{\mathrm{P}}$. The pose coverage, i.e., the fraction of reachable palm poses, is then

$$J_x = n_{\mathrm{reach}}^{\mathrm{m}} / n_{\mathrm{reach}}^{\mathrm{h}}. \tag{11}$$

*2) Velocity Coverage:* For a given reachable human arm configuration $\underline{q}^{\mathrm{h}} \in Q^{\mathrm{h}}\left(\mathbf{T}_{\mathrm{P}}^{\mathrm{S}}\right)$ and a corresponding manipulator configuration $\underline{q}^{\mathrm{m}} \in Q^{\mathrm{m}}\left(\mathbf{T}_{\mathrm{E}}^{\mathrm{B}}, \underline{p}\right)$, the set of required joint velocities can be calculated jointly using

$$\mathbf{A}\left(\underline{q}^{\mathrm{m}}, \underline{q}^{\mathrm{h}}\right) = \left(\mathbf{J}^{\mathrm{m}}\left(\underline{q}^{\mathrm{m}}\right)\right)^{-1} \begin{pmatrix} \mathbf{C}_{\mathrm{S}}^{\mathrm{B}} & \mathbf{0} \\ \mathbf{0} & \mathbf{C}_{\mathrm{S}}^{\mathrm{B}} \end{pmatrix} \mathbf{M}_v\left(\underline{q}^{\mathrm{h}}\right). \tag{12}$$

In this matrix, each column represents the manipulator joint velocities that are necessary to reach one of the principal axes of the velocity ellipsoid from Section V-C. To relate this with the maximum joint velocities,

$$\eta_v\left(\underline{q}^{\mathrm{m}}, \underline{q}^{\mathrm{h}}\right) = \min\left(1, \min_{i,j}\left(\frac{\dot{q}_{i,\max}^{\mathrm{m}}}{|A_{i,j}|}\right)\right) \tag{13}$$

is defined as a local measure for the velocity coverage. This expression is summed over all investigated poses resulting in

$$J_v = \frac{1}{n_{\mathrm{reach}}^{\mathrm{m}}} \sum_{\mathbf{T}_{\mathrm{P}}^{\mathrm{S}} \in W} \sum_{\underline{q}^{\mathrm{m}} \in Q^{\mathrm{m}}\left(\mathbf{T}_{\mathrm{E}}^{\mathrm{B}}, \underline{p}\right)} \sum_{\underline{q}^{\mathrm{h}} \in Q^{\mathrm{h}}\left(\mathbf{T}_{\mathrm{P}}^{\mathrm{S}}\right)} \eta_v \tag{14}$$

as a global and normalized measure for the velocity coverage. Note, that the first divisor is $n_{\mathrm{reach}}^{\mathrm{m}}$ instead of $n_{\mathrm{reach}}^{\mathrm{h}}$ to avoid the multiple penalization of poses that are not reachable with the analyzed manipulator parameters.

*3) Acceleration Coverage:* Until now, only the kinematic properties of the manipulator were considered. To incorporate dynamic properties, a simple mass model is introduced. Each joint motor is modeled as a point mass with a weight equal to its nominal weight $m_i^{\mathrm{m}}$ as stated in the datasheet [17] plus $20\,\%$ for the mounting structures. The links between the motors are represented by tubes with an outer diameter of $100\,\mathrm{mm}$, a wall thickness of $2\,\mathrm{mm}$ and a density of $4\,\mathrm{kgm}^{-1}$. The end effector is modeled as a solid cylinder with the same diameter, a length of $50\,\mathrm{mm}$ and a weight of $0.5\,\mathrm{kg}$.

Analogous to the velocity coverage and (6), the set of required accelerating joint torques can be approximated with

$$\mathbf{B}\left(\underline{q}^{\mathrm{m}}, \underline{q}^{\mathrm{h}}\right) = \mathbf{H}^{\mathrm{m}}\left(\underline{q}^{\mathrm{m}}\right)\left(\mathbf{J}^{\mathrm{m}}\left(\underline{q}^{\mathrm{m}}\right)\right)^{-1} \begin{pmatrix} \mathbf{C}_{\mathrm{S}}^{\mathrm{B}} & \mathbf{0} \\ \mathbf{0} & \mathbf{C}_{\mathrm{S}}^{\mathrm{B}} \end{pmatrix} \mathbf{M}_a\left(\underline{q}^{\mathrm{h}}\right) \tag{15}$$

for a given human arm configuration and its corresponding manipulator configuration. By neglecting the Coriolis term in the dynamics equation, a local measure for the acceleration coverage similar to (13) can be defined as

$$\eta_a\left(\underline{q}^{\mathrm{m}}, \underline{q}^{\mathrm{h}}\right) = \min\left(1, \min_{i,j}\left(\frac{\tau_{i,\max}^{\mathrm{m}}}{|B_{i,j}| + |\tau_{i,\mathrm{grav}}^{\mathrm{m}}|}\right)\right). \tag{16}$$

In this equation, $\underline{\tau}_{\mathrm{grav}}^{\mathrm{m}}\left(\underline{q}^{\mathrm{m}}\right)$ is the required torque for the compensation of gravity at the current manipulator configuration. Summation and normalization eventually yields the total acceleration coverage $J_a$, which has the same shape as (14), except that $\eta_a$ replaces $\eta_v$.

*4) Force/Torque Coverage:* To consider the requirement of isotropic forces and torques with the worst-case magnitudes $m_{\max} = 10\,\mathrm{Nm}$ and $f_{\max} = 50\,\mathrm{N}$, the matrix of principal force/torque directions is set to

$$\mathbf{M}_f = \begin{pmatrix} m_{\max}\mathbf{I} & \mathbf{0} \\ \mathbf{0} & f_{\max}\mathbf{I} \end{pmatrix}, \tag{17}$$

where $\mathbf{I} \in \mathbb{R}^{3\times3}$ is an identity matrix. The required joint torques for each column of $\mathbf{M}_f$ are the columns of

$$\mathbf{C} = \left(\mathbf{J}^{\mathrm{m}}\left(\underline{q}^{\mathrm{m}}\right)\right)^{\mathsf{T}} \mathbf{M}_f. \tag{18}$$

With this matrix, $\eta_f$ and $J_f$ are determined analogous to (14) and (16), except that $\mathbf{C}$ replaces $\mathbf{B}$ and $\eta_f$ replaces $\eta_v$.

*5) Constraints:* Design parameter constraints are necessary to restrict the solution space to feasible solutions and to limit the optimization effort. In the given scenario, the upper and lower bounds are set to $(0.3,0.3,0.3,0.3,0.12)\mathrm{m} \leq \underline{l}^{\mathsf{T}} \leq (1,1,1.5,1,0.3)\mathrm{m}$, $(3,3,1,1,1,1) \leq \underline{s}^{\mathsf{T}} \leq (3,3,3,3,3,3)$, and $(1,1,1,1,1,1) \leq \underline{r}^{\mathsf{T}} \leq (6,6,6,6,6,6)$. Here, the bounds for $\underline{l}$ were determined through geometrical considerations, which are reflecting designs that are apparently too big or too

small to be realized. The bounds for $\underline{s}$ and $\underline{r}$ originate from encoding the motor specifications in [17]. To complete the example, the additional constraint

$$s_i \geq s_{i+1} \quad \forall i \in \{1,2,...,5\} \tag{19}$$

is introduced to prevent non-monotonous joint sizes.

### B. Optimization

Finding the global maximum of (9) is challenging because a nonlinear, non-convex mixed-integer problem is to be solved. Moreover, gradient information is not straightforward to obtain since standard algorithms for the calculation of the inertia matrix and the Jacobian do not provide derivatives. Although a perfect global minimization is not necessary to achieve satisfactory results, the optimization algorithm must cope with local extrema. For these reasons, a mixed-integer genetic algorithm is selected as a suitable optimizer. This offers the additional advantage of upscalable parallelization.

### C. Implementation

The previously described problem and its optimizer, which is based on a genetic algorithm, were implemented using Matlab and its Global Optimization Toolbox. To guarantee reliable and fast calculations of the IK of the human arm, ikfast [18] is deployed. The Jacobian, the inertia matrix, and the gravity-compensating torque are all calculated using the Matlab Robotics System Toolbox. For the IK of the haptic manipulator, a hand-crafted closed-form solution is utilized.

## VII. Results

Motivated by the rotationally symmetric workspace of the haptic manipulator, the first joint is placed $0.61\,\mathrm{m}$ above the user's shoulder throughout the following evaluation. This results in $\underline{x}_{\mathrm{S}}^{\mathrm{B}} = (0,0,-0.61)^{\mathsf{T}}\mathrm{m}$ and $\mathbf{C}_{\mathrm{S}}^{\mathrm{B}} = (0,-1,0;0,0,1;-1,0,0)$. The user's palm is directly coupled with the end effector of the manipulator through $\mathbf{C}_{\mathrm{E}}^{\mathrm{P}} = (0,0,1;0,-1,0;1,0,0)$. The offset $\underline{x}_{\mathrm{E}}^{\mathrm{P}}$ is set to zero. The workspace of the human arm is sampled with a resolution of $0.1\,\mathrm{m}$. At each point, 505 orientations are evaluated.

With this setup in combination with a population size of 200, the optimization run times on a server with an Intel Xeon Gold 6230 CPU (40 cores) ranged from 10 to 29 hours. The results were not influenced significantly by modified replication parameters, an increased angular resolution, or weaker stopping criteria. In total, 31 runs of the optimization were performed. While the objective function consistently remained between $2.236$ and $2.245$, the position of the maximum varied due to the stochastic nature of the genetic algorithm. Therefore, different solutions exhibit distinct contributions to the terms specified in Section VI-A.

An analysis using k-means clustering and the average silhouette score reveals that the three clusters listed in Table III exist among the solutions. The average of the euclidean distance between optimized link lengths $\underline{l}$ and cluster centroids (i.e., the intra-cluster deviation) is $6.5\,\mathrm{mm}$. Compared to the average distance of the cluster centroids with respect to the overall mean (i.e., inter-cluster deviation), which is $58\,\mathrm{mm}$, this indicates that all solutions within a cluster correspond to a cluster-specific local extremum. Although the observed clusters do not guarantee that no additional maxima exist, they provide a reduced set of *optimal trade-offs*. At this point, it is required to favor one of the coverage quantities in the overall objective function in order to get a final design. Here, we choose the pose coverage as the most important factor, because unreachable poses will become completely inaccessible for the haptic rendering. In contrast, a reduced acceleration or velocity coverage will just limit the achievable transparency for the affected poses.

### A. Coverage

The accepted design parameters for the haptic manipulator are printed in bold in Table III. Fig. 5(a) shows the resulting spatial distribution of the pose coverage, which exhibits values close to one at chest height of the user. Poses that are very high or very low relative to the chest are less reachable due to the limited length of the fourth link $l_4$. Similar to the position coverage, the velocity coverage in Fig. 5(b) deteriorates when the goal pose is rather high or low. The reason for this is the singularity that occurs when $q_4$ approaches $0°$ or $180°$.

In general, increasing $l_4$ would overcome both limitations and yield an increase of $J_x$ and $J_v$, but longer link lengths would sacrifice the acceleration capabilities in turn. This is confirmed by the acceleration coverage, which is the lowest among all clusters in Table III. A closer look at Fig. 5(c) reveals, that the acceleration coverage is lower for poses with manipulator configurations close to $q_4 = 90°$. One possible explanation for this is the gravity compensation torque of approximately $21\,\mathrm{Nm}$ for joint 4 in this state, which takes up a significant portion of the joint's peak torque.

For the desired isotropic forces and torques, the selected design is ideal as it facilitates a coverage of $100\,\%$. This implies, that the force/torque coverage is not the crucial aspect regarding the overall manipulator performance.

### B. Validation

In order to verify that the proposed manipulator design procedure is also effective for real-world scenarios, a validation of the selected parameter set using real-world data from [19] was conducted. The selected dataset contains 9 hours of full-body skeleton tracking data that was captured from 13 subjects performing various activities such as cooking, laundry, and cleaning. In the first validation step, the pose of the right hand relative to the shoulder of the subjects is extracted to remove the effects of locomotion and other whole-body movements. Then, the data is smoothed with a fourth-order Butterworth filter with a cut-off frequency of $5\,\mathrm{Hz}$ and differentiated twice numerically. After each differentiation, the smoothing filter is reapplied. The resulting pose, velocity, and acceleration profiles are then fed back into the optimized manipulator model. For each time step, the IK of the manipulator, the necessary joint velocities and the necessary joint torques are calculated based on the full kinematic and dynamic model.

For the selected manipulator design, the whole dataset with a duration of 9 hours was evaluated. Across all 13 subjects and all activities (e.g., cooking, laundry, eating), $94.0\,\%$ of the tested hand poses were reachable with the haptic manipulator. The velocity of the hand was fully achievable in $93.7\,\%$ of all

| Cluster # | # of runs | $J$ | $J_x$ | $J_v$ | $J_a$ | $J_f$ | $\underline{l}$ in cm | $\underline{s}$ | $\underline{r}$ |
|---|---|---|---|---|---|---|---|---|---|
| 1 | 10 | 3.238 | 0.811 | 0.882 | 0.545 | 1.000 | (50.2, 64.3, 79.9, 37.5, 12.0) | (3, 3, 2, 2, 1, 1) | (2, 2, 2, 2, 2, 2) |
| 2 | 14 | 3.245 | 0.717 | 0.775 | 0.753 | 1.000 | (50.8, 59.0, 75.0, 32.3, 12.0) | (3, 3, 2, 2, 1, 1) | (3, 2, 2, 2, 2, 2) |
| **3** | **7** | **3.244** | **0.879** | **0.882** | **0.483** | **1.000** | **(52.9, 66.8, 75.2, 42.3, 12.0)** | **(3, 3, 2, 2, 1, 1)** | **(2, 2, 2, 2, 2, 2)** |

TABLE III: Clusters, which represent optimal trade-offs, within the results of 31 optimization runs.

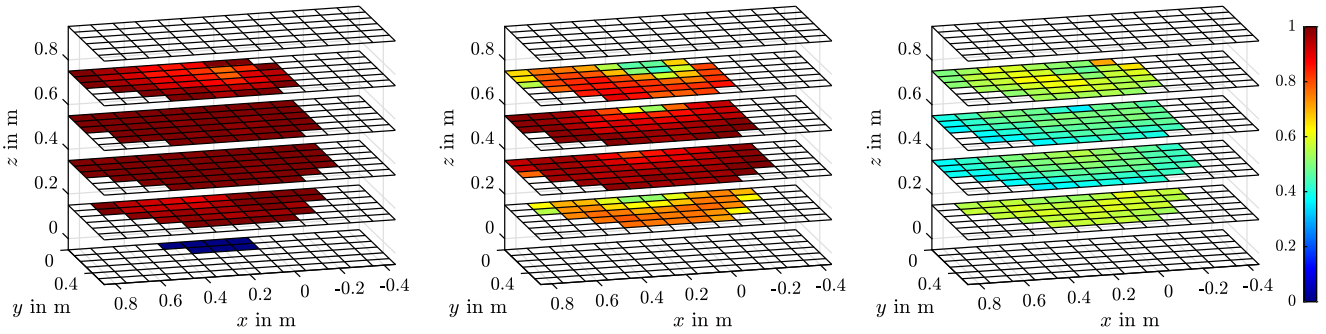


(a) Pose coverage $J_x$. (b) Velocity coverage $J_v$. (c) Acceleration coverage $J_a$.

Fig. 5: Spatial distributions of the different coverage terms for the final parameter set. A value of zero indicates that the given property is not covered at all, while a value of one indicates that it is covered entirely. The perspective is identical with Fig. 3.

samples including those that were not reachable at all. Similarly, $90.1\,\%$ of the recorded accelerations were within the limits of the haptic manipulator. The standard deviations for these performance measures across the individual subjects are $4.15\,\%$, $4.15\,\%$, and $4.41\,\%$, respectively. This demonstrates that the proposed optimization algorithm indeed creates a reasonable and versatile manipulator design, which is robust towards parameter variations emerging from different subjects.

Further validation is enabled through a virtual prototype. For this, the user's hand pose and its derivatives are captured in real-time by an HTC Vive tracking system and fed into the full kinematic and dynamic model to calculate the necessary joint angles, speeds, and torques. These values are then compared with the joint capabilities and the result is visualized online using an extended reality device. As a result, engineers and users can intuitively test the behavior of the designed manipulator. We refer the reader to the supplementary material for a demonstration of this feature.[2]

## VIII. Conclusions

In this paper, an optimization-driven design approach for general-purpose kinesthetic haptic interfaces was presented. Without any particular assumptions about the task that is to be performed with the haptic interface, the proposed method generates several possible compromises of equal value with different strengths and weaknesses regarding pose, velocity, and acceleration coverage. The effectiveness of one of the discovered designs was validated using a complex real-world data set. Accordingly, good real-world performance of the haptic manipulator can be expected.

In future work, the selected optimal design will be transitioned into a real manipulator prototype. Regarding the actual optimization process, the underlying manipulator model will be improved, so that features such as joint losses, motor inertia, and material properties are taken into account. Furthermore, the human arm model should be improved to increase resemblance with the real human arm. Eventually, the presented approach can be generalized regarding redundant haptic interfaces and the general problem of robotic manipulator design.

[2] https://youtu.be/LSu-HVIHxzQ

## References


[1] M. Ueberle, "Design, control, and evaluation of a family of kinesthetic haptic interfaces," Ph.D. dissertation, Tech. Univ. of Munich, 2006.

[2] Y. Zimmermann, A. Forino, R. Riener *et al.*, "ANYexo: A versatile and dynamic upper-limb rehabilitation robot," *IEEE Robot. Autom. Let.*, vol. 4, no. 4, pp. 3649–3656, Oct. 2019.

[3] J. C. Perry, J. M. Powell, and J. Rosen, "Isotropy of an upper limb exoskeleton and the kinematics and dynamics of the human arm," *Appl. Bionics and Biomechanics*, vol. 6, no. 2, pp. 175–191, Jun. 2009.

[4] F. Zacharias, I. S. Howard, T. Hulin *et al.*, "Workspace comparisons of setup configurations for human-robot interaction," in *2010 IEEE/RSJ Int. Conf. on Intell. Robots and Systems*, Oct. 2010, pp. 3117–3122.

[5] T. Yoshikawa, "Manipulability of robotic mechanisms," *Int. J. Robot. Research*, vol. 4, no. 2, pp. 3–9, Jun. 1985.

[6] ——, "Dynamic manipulability of robot manipulators," in *Proc. 1985 IEEE Int. Conf. on Robot. Autom.*, Mar. 1985, pp. 1033–1038.

[7] L. J. Stocco, S. E. Salcudean, and F. Sassani, "Mechanism design for global isotropy with applications to haptic interfaces," in *Proc. ASME Winter Annual Meeting*, vol. 61, Nov. 1997, pp. 115–122.

[8] O. Khatib and J. Burdick, "Optimization of dynamics in manipulator design: The operational space formulation." *Int. J. Robot. Autom.*, vol. 2, no. 2, pp. 90–98, 1987.

[9] M. Chadwick, H. Kolvenbach, F. Dubois *et al.*, "Vitruvio: An open-source leg design optimization toolbox for walking robots," *IEEE Robot. Autom. Let.*, vol. 5, no. 4, pp. 6318–6325, Oct. 2020.

[10] A. Pérez Arias, "Haptic guidance for extended range telepresence," Ph.D. dissertation, Karlsruhe Inst. of Technol., 2013.

[11] D. A. Winter, *Biomechanics and Motor Control of Human Movement*, 4th ed. Hoboken, NJ, USA: Wiley, 2009.

[12] *DIN 33402-2:2020-12: Ergonomics – Human body dimensions – Part 2: Values*, German Inst. for Standardization Std., 2020.

[13] J. Rosen, J. Perry, N. Manning *et al.*, "The human arm kinematics and dynamics during daily activities – toward a 7 DOF upper limb powered exoskeleton," in *Proc. 12th Int. Conf. on Adv. Robot.*, Jul. 2005, pp. 532–539.

[14] I. A. Kapandji, *The physiology of the joints*, 5th ed. Churchill Livingstone, 2002, vol. 1.

[15] J. L. Pons, *Wearable Robots: Biomechatronic Exoskeletons*. Chichester, England: Wiley, 2008.

[16] D. Frisch and U. D. Hanebeck, "Deterministic gaussian sampling with generalized fibonacci grids," in *Proc. 24rd Int. Conf. on Inf. Fusion (Fusion 2021)*, Nov. 2021, to appear.

[17] Sensodrive GmbH. (2021, Sep.) SENSO-Joints. [Online]. Available: www.sensodrive.de/products/torque-technology-senso-joint.php

[18] R. Diankov, "Automated construction of robotic manipulation programs," Ph.D. dissertation, Carnegie Mellon Univ., 2010.

[19] A. Saudabayev, Z. Rysbek, R. Khassenova *et al.*, "Human grasping database for activities of daily living with depth, color and kinematic data streams," *Scientific Data*, vol. 5, no. 1, May 2018.